An experimental investigation on cemented sand particles using different loading paths: Failure modes and fabric quantifications

Wanying Wang [a], Deheng Wei [b,*], Yixiang Gan [b]

[a] *School of Civil and Transportation Engineering, Guangdong University of Technology, Guangzhou, China*
[b] *School of Civil Engineering, The University of Sydney, Sydney, Australia*

HIGHLIGHTS

- Fracture of cemented sands was investigated experimentally under different loads.
- Distinctively macro fracture modes were induced by different loading directions.
- A multi-scale rotational HWT method was proposed to quantify fracture surface fabric.

ARTICLE INFO

ABSTRACT

Cemented sands are not only widely found in nature, but also artificially made broadly for various engineering applications. We experimentally studied underlying breakage behaviour of artificially cemented sands under different loading paths at particle scale. Two types of sands (Leighton Buzzard sand and crushed limestone particles) and two types of bond materials (gypsum plaster and Portland cement) were used to prepare artificially cemented particles. Three typical loading paths, resulting in different breakage modes of specimens, including (1) uniaxial compression, (2) combined compression-pure shear (shorted by 'pure shear') and (3) combined compression-shear-bending (shorted by 'bending') were applied. It was found that when catastrophic failure occurred, cracks propagated roughly parallel to the loading axis in both particles and their bridging cementation in uniaxial compression tests. While under pure shear loads, the macroscopic fracture initiated at and evolved along particle-bond interfaces. By contrast, bending moment induced shear bands of which crack planes only occurred in cementation and were nearly parallel to each other in bending tests. For the intact samples before compression tests as well as fragmentations after breakage, Scanning Electron Microscope (SEM) images were taken for samples prepared by four kinds of materials, and multiscale rotational Haar Wavelet Transformation (HWT) was implemented to quantify their fabric including fabric value and direction. It is concluded that fracture surfaces of particle materials had more distinct fabric than intact particle surface. Meanwhile, due to sliding shear-dominant longitudinal bond fracture surfaces had more evident fabric than their corresponding tensile-dominant horizontal fracture surfaces. Consequently, our developed apparatus combined with the fabric quantification method sheds new light on cemented granular materials at the particle scale.

© 2020 Elsevier Ltd. All rights reserved.

1. Introduction

Cemented sands, bridged by cementation matrix, sharing microscopic processes via interfaces in control of their macroscopic behaviour can be divided into two categories, namely artificially and naturally cemented granular materials [33]. Similar to concrete, cemented sands are composed of three phases, namely, sand, cementation, and interfacial transition zone (ITZ) between the two.

It is widely accepted that ITZ is the weakest phase among the three. Cementation in nature can be combinations of calcite, quartz, iron oxides and clay, such as sedimentary rocks [40]. Artificially cemented sands have an extensive range of applications including concrete, recycling construction materials, asphalts, cemented paste backfill and bio-grouted soils, across the broader field of engineering [26,46,29,30,3]. In geotechnical engineering, because many natural sands are weakly cemented, mixtures of cementation and soil have been widely used for enhancing soil strength [2] and liquefaction resistance [36], such as building stable foundations and strengthening slopes [30]. Among a large

---

number of studies for characterization of cemented sand structures of which inelasticity is due to grain crushing, cementation disintegration and reorganization of fragments, it is well accepted that the major two dominant factors are bonding and fabric [11,17].

There are three mainstream methods to investigate cemented sands: experimental (e.g., [27,20,8], analytical (e.g., [37,31,19] and numerical approaches (e.g., [45,43,44,14,15]. In the last decades, experimental studies may be the most commonly implemented, and many contributions have been made: (i) the presence of bonding could make sandy soil structures more stable and, thus increase their stiffness and strength [3,24]; (ii) under identical triaxial loading, the sample response shows less contraction or more dilation with cementation as compared with clean sands [12,28]; (iii) the critical state parameters seem to be independent of the cementation level when stresses are more than the apparent pre-consolidation stress [9,20]; and (iv) with the debonding-induced stiffness degradation, post-peak behaviours become more brittle, and significant fracture or breakage of bonding material appears accompanying the initiation of yielding [44]. However, contributions from the particle scale, e.g. a bond is sandwiched by two particles, as one set of most fundamental elements in cemented sands, can be seldomly found. Based on experimental studies for parameters calibration, many constitutive models have been proposed for accounting the breakage of cemented sands, and most of them are focused on bonding degradation [25,48], so does some numerical discrete element modelling [13,37]. Only considering bonding failure is evidently problematic, because all three phases can fracture and attribute to the final complete fracture surface [21,49]. To tackle this issue, based on recently developed breakage mechanics [16], Tengattini et al. [39] propose a novel thermodynamics-based constitutive model coupling grain crushing and cement disintegration. However, as the weakest phase compared with sand and cementation, the interface fracture is not considered in their model. Although breakage of both bond and particle is not covered, Zhao and Gao [17] propose an elasto-plastic constitutive model on cemented granular materials with strong sands, as the first step towards uncovering fabric constitutively. Nevertheless, too many parameters exist in analytical models and some of them lack the intrinsic physical meaning, which hiders their wide applications.

Due to the limitations of experiments and analytical solutions, numerical methods are alternative in quantitatively characterizing micro mechanics of cemented sands. Discrete element method (DEM) has been mostly implemented for cemented sands in geotechnical engineering (e.g., [34,22,10]. However, to the best knowledge of the authors DEM seems not very suitable for simulating breakage behaviour of cemented sand. For example, spherical particles are bridged by bonds, while the bond in DEM has been usually simplified as a thickness-free interface; that is to say there is no cementation mass in the cemented granular sample. Furthermore, basic elements in classical DEM are regarded as rigid bodies, hence deformations of which are the key to breakage cannot be considered. More importantly, this type of DEM cannot even effectively reproduce the simplest bulk elastic behaviour defined just by two common parameters, elastic modulus and Possion's ratio, because these apparent properties are dependent on both mechanical and structural properties (local coordinate numbers of the rigid sphere element) [6,4]. Wong and Wu [45] proposed finite element method (FEM) to simulate normal compression behaviour of a cemented sand in 2D using two idealized circles. Although particles and their bridging bond are ideally connected without interface elements, they found the normal stiffness and maximum tensile stress are both significantly influenced by the thickness of the bond.

Based on aforementioned research, we are motivated to revisit the breakage behaviour of cemented sands under different loading paths experimentally. Fracture surfaces of particles and bonding materials are examined with the aid of SEM images, of which the fabric is quantified by multi-scale rotational Haar Wavelet transformation (HWT). The paper is organized as follows. In Section 2, our newly developed equipment and examined materials are introduced. In Section 3, the image process, in terms of multi-scale rotational HWT, is illustrated. Different fracture mechanics inducing diverse fabric can be analysed. Results about fracture patterns under three kinds of loading paths and their associated mechanical responses and fabric are presented in Section 4. Finally, the main conclusions of this study are summarized in Section 5.

2. Experiments

In this study, a group of artificially cemented sand particles were tested under different loading paths, including uniaxial compression, pure shear with or without bending moment, as shown in the schematic illustration of Fig. 1. Fig. 1a shows the uniaxial compression tests along vertical directions, in which a pair of axial force applied along the vertical central axis of the cemented grains. In Fig. 1b, a pair of cemented grain is held by a certain normal force, and then another pair of horizontal force is applied along the horizontal central axis of the bond. In this case, the cemented grain is in a combined compression and shearing. When the horizontal forces move along vertical and opposite direction, which means there is an eccentric distance e_0, the specimen is tested on compression, shearing as well as bending (Fig. 1c).

The loading apparatus developed is shown in Fig. 2 [42]. The system consists of a supporting frame, two stepper motors with controllers, two load cells with a capacity of 1000 N (sensitivity of 2 mV/V and accuracy of 0.15%), four high-resolution Linear Variable Differential Transformers (LVDTs) with a resolution of 0.1 micros, a sensitivity of 375 mV/V and an accuracy of 0.25%, and a digital microscope camera. The two stepper motors are fixed along orthogonal directions to supply normal and shear forces, respectively. They are in the control of force or displacement by a custom-built program. When the cemented grain is under compression, the force is applied by the vertical linear actuator with a loading speed of 0.2 mm/hour. While the specimen is tested under compression-shearing or compression-shearing-bending loading paths, the shear force is applied by the horizontal linear actuator with a loading speed of 0.2 mm/hour, and the vertical linear actuator applies the constant normal force in a force-controlled manner. Two load cells were assembled with each actuator to measure the forces along the orthogonal directions. The artificial cemented particles were held by a pair of L-shape mounts, which allowed the external horizontal force applied on the vertical arms. Both the upper and lower mounts could move freely along the horizontal loading axis. Besides, both mounts were connected to the upper and lower parts of the apparatus by pin joints, allowing the bending moment applied on the specimen. During the combined compression-shear tests (shorted as "pure shear") and combined compression-shear-bending tests (short as "bending"), the horizontal force was applied on the arm of upper L-shape mount by a loading end, while the lower L-shape mount was the reaction end. Two pairs of LVDTs were used in this apparatus. One pair was fixed symmetrically to the vertical loading axis with a spacing of 16 mm. The armatures of the other pair of LVDTs were glued on the arm of the upper mount, which were symmetrical to the horizontal loading axis and 8 mm apart. The vertical and horizontal displacements could be obtained from the average readings from each pair of LVDTs, respectively. The rotation angle during the bending tests could be calculated by the difference in readings from the horizontal LVDTs and the distance between them by a simple geometric relationship. A digital microscope camera was
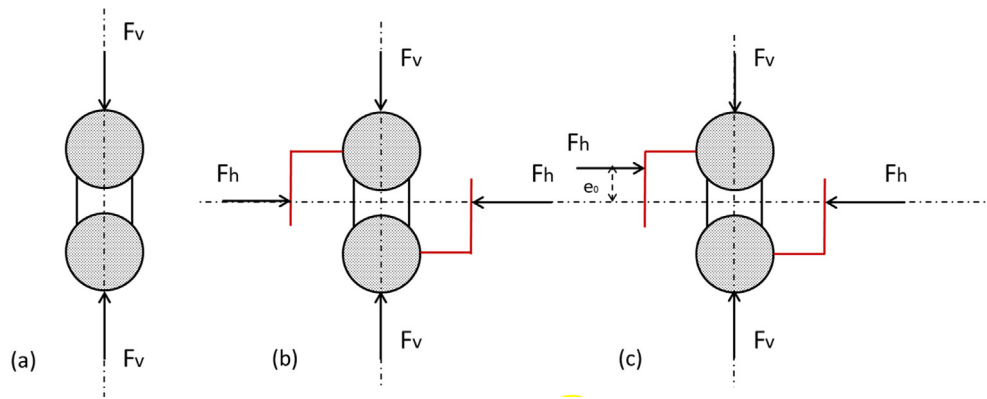
Fig. 1. Schematic illustration of tests artificially cemented particles under different loading paths: (a) compression (b) combined compression and shear (c) combined compression, shear and bending.
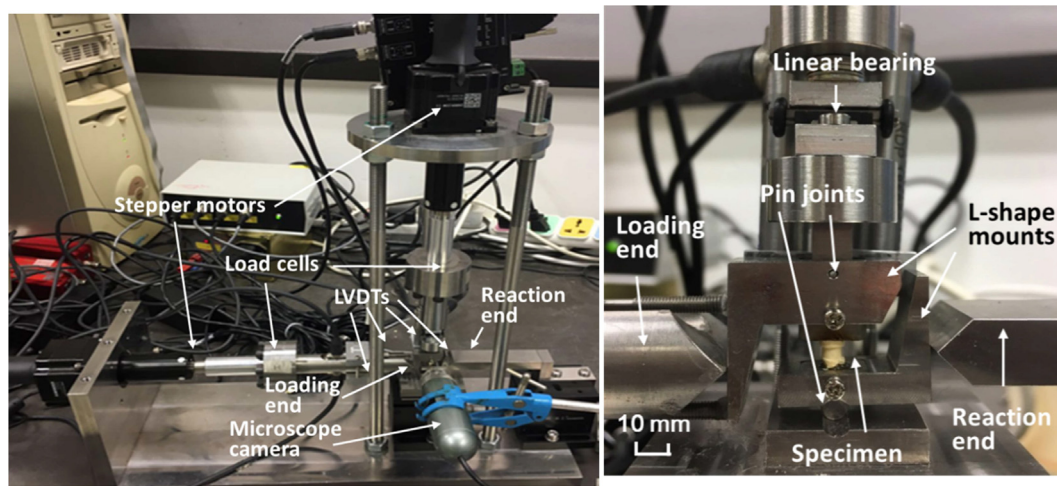

Fig. 2. (a) Apparatus used in tests for artificially cemented particles under complex loading paths (b) details for the loading part.

used to capture the failure behaviour of the cemented particles in different loading paths. The details of the loading part are shown in Fig. 2b.

LBS particles and crushed limestone, of size 2.36–5.00 mm, were used. The former is a silica sand from the United Kingdom (UK) and with high degree of roundness and smooth texture, due to geological transportation process. While the latter is a diagenetic rock with rectangular sections, relatively angular particle surfaces and many internal flaws or fractures resulting from the crushing. Two types of bonding materials, Portland cement and gypsum plaster (Crystacal D from the UK), were used to cement single grains to investigate the effect of different bonding materials. The two bonding materials, gypsum and Portland cement, were prepared with their optimal water contents of 25% and 40% as suggested by manufacturers, respectively, after waiting for at least 24 h for fully hardening. Artificially cemented particles with such procedures could represent, perhaps, weakly cemented sands or young clastic rock. The unit artificially cemented particles were prepared and equipped using a pair of containers made of Perspex, with a bond thickness of 2 mm named of "thick bond" as defined by Jiang et al. [23]. Notably, in Wong and Wu [45]'s FEM simulations, both bond thickness and cross-section area can significantly influence global strength of unit cemented sands. In this study, we aim to investigate different failure modes induced by competition fracture mechanism among three phases, hence care must be taken to convince mass of cementation bond is not much far from that of

sand particles. Consequently, bond thickness and cross-section area are nearly identical to those of sand particles, as shown later in Fig. 9.

According to Wang et al. [41], using gypsum plaster as the bonding material gave more constant results, in terms of force–displacement relationship curve for loading tests, compared with Portland cement. Simultaneously, because of the stress concentration induced by angular morphology features and more internal flaws due to crushing, crushed limestone tended to be fractured prior to the bond and even ITZ. As a result, no wanted competition mechanism among three phases occurred. To bypass this problem, although the implemented bond was the thinnest for adequate cementation process, limestone grains could still fracture before other two phases. Therefore, for such competition mechanism, only cemented sands, composed of LBS particles and gypsum plaster, were emphasized for the mechanical responses in this study. As for the other types of cemented particles, only scanned using SEM for fabric quantification was conducted for intact samples before tests as well as debris after compressive loading tests.

3. Fabric quantification for fractured surfaces

The Haar Wavelet transformation (HWT), originally proposed by Haar [18], has been most widely used in image compression. Additionally, as a novel and all-round image processing technique HWT can also be applied in image segmentation, edge detection,

denoising, and feature and texture analysis. In geotechnical applications, HWT has been successfully applied in detecting soil particle size distribution [38,32], roughness [9] and fabric tensor [50,51]. HWT could be introduced from a 2×2 pixels grey image:

$$I(x,y) = \begin{bmatrix} i & j \\ k & l \end{bmatrix} \tag{1}$$

where x and y denote the point positions in the whole grey image and belong to 1 or 2 in this 2×2 pixels grey image; i, j, k and l are grey values from 0 (black) to 1 (white). The HWT for this squared image is:

$$I_{HWT}(x,y) = \begin{bmatrix} A(x,y) & H(x,y) \\ V(x,y) & D(x,y) \end{bmatrix} = \begin{bmatrix} \frac{(i+j)+(k+l)}{2} & \frac{(i+j)-(k+l)}{2} \\ \frac{(i+k)-(j+l)}{2} & \frac{(i+l)-(j+k)}{2} \end{bmatrix} \tag{2}$$

where $A(x,y)$ is the downscaling of $I(x,y)$ by factor 2; $V(x,y)$, $H(x,y)$ and $D(x,y)$ are the average differences in vertical, horizontal and diagonal directions, respectively. An important property of HWT is the invariant tensorial property, defined as energy, during transformation. The energy $E_{I(x,y)}$ reads:

$$E_{I(x,y)} = \sum_{x=1}^{2} \sum_{y=1}^{2} [I(x,y)]^2 = i^2 + j^2 + k^2 + l^2 \tag{3}$$

And it can be easily obtained:

$$E_{I(x,y)} = E_{I_{HWT}(x,y)}$$
$$i^2 + j^2 + k^2 + l^2 = \left[\frac{(i+j)+(k+l)}{2}\right]^2 + \left[\frac{(i+j)-(k+l)}{2}\right]^2 + \left[\frac{(i+k)-(j+l)}{2}\right]^2 + \left[\frac{(i+l)+(j+k)}{2}\right]^2$$
$$i^2 + j^2 + k^2 + l^2 = E_A + E_H + E_V + E_D \tag{4}$$

where E_A, E_H, E_V and E_D are the energy subsets of $E_{I_{HWT}(x,y)}$. Accordingly, E_H and E_V denote the differences in horizontal and vertical directions of the transformed image.

For a 4×4 image ($A_0(x,y)$), it can be downscaling into 2×2 image for the first time HWT performed on every adjacent sub 2×2 image:

$$A_0(x,y) = \begin{bmatrix} i & j & k & l \\ m & n & o & p \\ q & r & s & t \\ u & v & w & x \end{bmatrix} \tag{5}$$

$$A_1(x,y) = \begin{bmatrix} \frac{(i+n)+(m+j)}{2} & \frac{(k+p)+(o+l)}{2} \\ \frac{(q+v)+(u+r)}{2} & \frac{(s+x)+(w+t)}{2} \end{bmatrix} \tag{6}$$

And if HWT is continually conducted on $A_1(x,y)$:

$$A_2(x,y) = \left[\frac{(i+n)+(m+j)+(k+p)+(o+l)+(q+v)+(u+r)+(s+x)+(w+t)}{4}\right] \tag{7}$$

Given a $2^M \times 2^M (M \in N^*)$ image, HWT can be done for M times for it and its associated vertical and horizontal energies for the i-th HWT are E_{V_i} and E_{H_i}, respectively. Fig. 3 illustrates an original SEM image of a fractured LBS particle and its seven levels of HWT-generated images. Then, follow Zheng and Hryciw [50], the maximum of energy of the two are defined:

$$E_{V_{max}} = \max(E_{V_1}, \quad E_{V_2}, \quad \dots \quad E_{V_{M-1}}, \quad E_{V_M})$$
$$E_{H_{max}} = \max(E_{H_1}, \quad E_{H_2}, \quad \dots \quad E_{H_{M-1}}, \quad E_{H_M}) \tag{8}$$

Perpendicular to the fabric direction of fracture surfaces, grey values of SEM images change most and produce maximum energy. That means searching for the direction of fracture fabric is changed to that of maximum/minimum energy direction. However, HWT only quantifies horizontal and vertical direction energies considering diagonal energies are of limited values. Rotational Haar Wavelet transformation (RHWT) proposed by Zheng and Hryciw [53,51] was applied to rotate the original image for computing fabric tensors towards more rounded directions (Fig. 4). An energy ratio is defined:

$$ER(\theta) = \frac{2}{\pi} \arctan\left[\frac{E(\theta + 90°)}{E(\theta)}\right] = \frac{2}{\pi} \arctan\left(\frac{E_{V_{max}}}{E_{H_{max}}}\right) \tag{9}$$

where $\theta \in [0°, 360°)$ is the rotation angle of the original image. Due to the symmetry of rotating, $ER(\theta) = ER(180° + \theta)$ can be obtained.

A_0: 256×256 A_1: 128×128 A_2: 64×64 A_3: 32×32

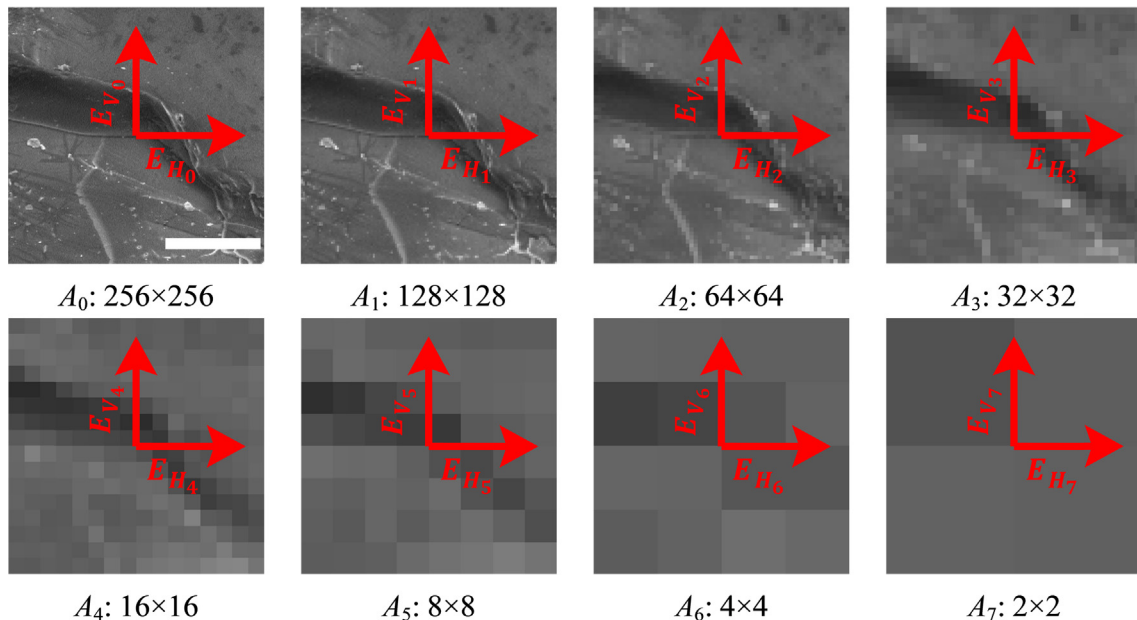A_4: 16×16 A_5: 8×8 A_6: 4×4 A_7: 2×2

Fig. 3. A_0, a fractured LBS fracture surface, and its seven levels of Haar Wavelet transformation. The two arrows denote energies with respect to vertical ($E_{V_{i-th}}$) and horizontal ($E_{H_{i-th}}$) directions. i-th means the number of times for downscaling of the original image. The scale bar in it represents 100 μm.
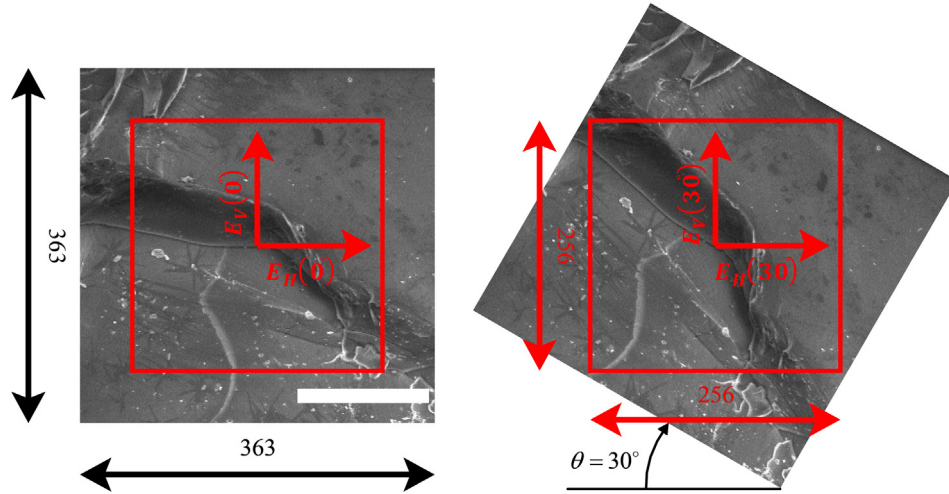
Fig. 4. Rotational Haar Wavelet transformation for an SEM image of LBS fracture surface of 363 × 363 pixels. The red square denotes the zone of 256 × 256 pixels for quantifying vertical and horizontal energies during rotation. θ is for the rotation angle. The scale bar in it represents 100 μm. (For interpretation of the references to colour in this figure legend, the reader is referred to the web version of this article.)

Simultaneously, due to $E_{V_{max}}(\theta) = E_{H_{max}}\left(\theta + 90^{\circ}\right)$ and $E_{H_{max}}(\theta) = E_{V_{max}}\left(\theta + 90^{\circ}\right)$, if $ER(\theta)$ is known for $\theta \in [0^{\circ}, 90^{\circ})$, $ER(\theta)$ of the full range $\theta \in \left[0^{\circ}, 360^{\circ}\right)$ is known. For simplicity, the continuum $ER(\theta)$ function is discretized by 1° increments from 1° to 360°, and 90 $ER(\theta)$ values $(ER\left(0^{\circ}\right), ER\left(1^{\circ}\right), ER\left(2^{\circ}\right) \cdots, ER\left(89^{\circ}\right))$ are sufficient for the full scope. Notably, from Fig. 4 it is evident that during the rotation process, where the subareas are rotated clockwise, the certain central $2^{M} \times 2^{M}$ window must be fully contained in the rotated image. Hence, the minimum size of the original or rotated image is $2^{M+0.5} \times 2^{M+0.5}$ for $2^{M} \times 2^{M}$ sized window.

The image noise and multiscale morphology features of fracture surface may influence the image fabric direction, therefore the second order Fourier series is implemented to make it more obvious visually *via* fitting its distribution $ER(\theta)$:

$$ER(\theta) = 0.5 + a \cdot \cos(2\theta) + b \cdot \sin(2\theta) \tag{10}$$

where a and b are Fourier coefficients determined by $ER(\theta)$ using the least square fitting method, as shown in Fig. 5. Eq. (10) can also be written as:

$$\begin{aligned} ER(\theta) &= 0.5 + \sqrt{a^2 + b^2}\sin(\beta + 2\theta) \\ \sin\beta &= \frac{a}{\sqrt{a^2+b^2}} \\ \cos\beta &= \frac{b}{\sqrt{a^2+b^2}} \end{aligned} \tag{11}$$

Thus, the maximum and minimum $ER(\theta)$ are calculated:

$$\begin{bmatrix} ER_{\max} \\ ER_{\min} \end{bmatrix} = 0.5 \pm \sqrt{a^2 + b^2} \tag{12}$$

For example, the determined Fourier coefficients of the LBS fracture surface are $a = 0.0776$ and $b = -0.0604$; the maximum and minimum fabric scalar are 0.598 and 0.402; the direction of ER_{max} is towards 162°, highlighted in Fig. 5. For an ideal complete isotropic fabric, the ER yields a circle of radius equal to 0.5 in Fig. 5. Generally, fabric of a specific image is quantified by and compressed into 2 values, namely the fabric value ER_{max} and fabric direction ER_{max} is oriented.

In Zheng and Hryciw [50], only one original $2^{M+0.5} \times 2^{M+0.5}$ SEM image is selected for once RHWT to determine the fabric direction, however it is somewhat coarse regarding the multiscale morphol-
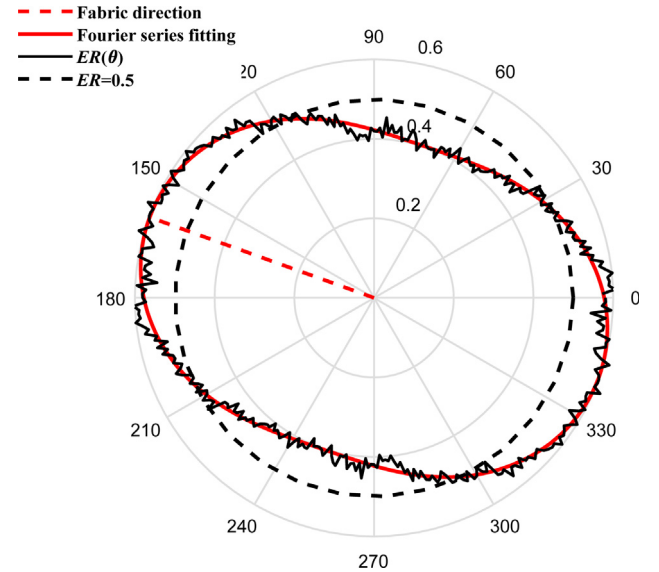

Fig. 5. Results in polar coordinate system of RHWT on the LBS fracture surface in Fig. 4.

ogy features presented. Based on the above description, we propose here a multiscale RHWT to detect fabric direction of the SEM images of cemented sand fracture surface; that is, the large image is divided into subareas and RHWT is performed on each of them. As shown in Fig. 6, the image is divided into $N \times L$ minor parts, each of which has more than $2^{M+0.5} \times 2^{M+0.5}$ pixels. Then the $ER_{all}(\theta)$ of the whole image is defined by the sum of those of subareas at corresponding angle θ_i:

$$ER_{all}(\theta_i) = \sum_{i=1}^{N \times L} \frac{ER(\theta_i)}{N \times L} \tag{13}$$

where $\theta_i = 0^{\circ}, 1^{\circ}, 2^{\circ} \cdots 179^{\circ}$. Notably, the size of subarea has great influence on the resulting fabric direction and value, thus the values of M selected subarea size is 2, 3, 4, 5, 6 and 7, considering the SEM images used in this study have 712 × 423 pixels. After the accumulated distribution of $ER_{all}(\theta)$ is obtained, the second Fourier series in Eq. (10) is then applied to fit it. Fig. 6 and Fig. 7 illustrate the repre-
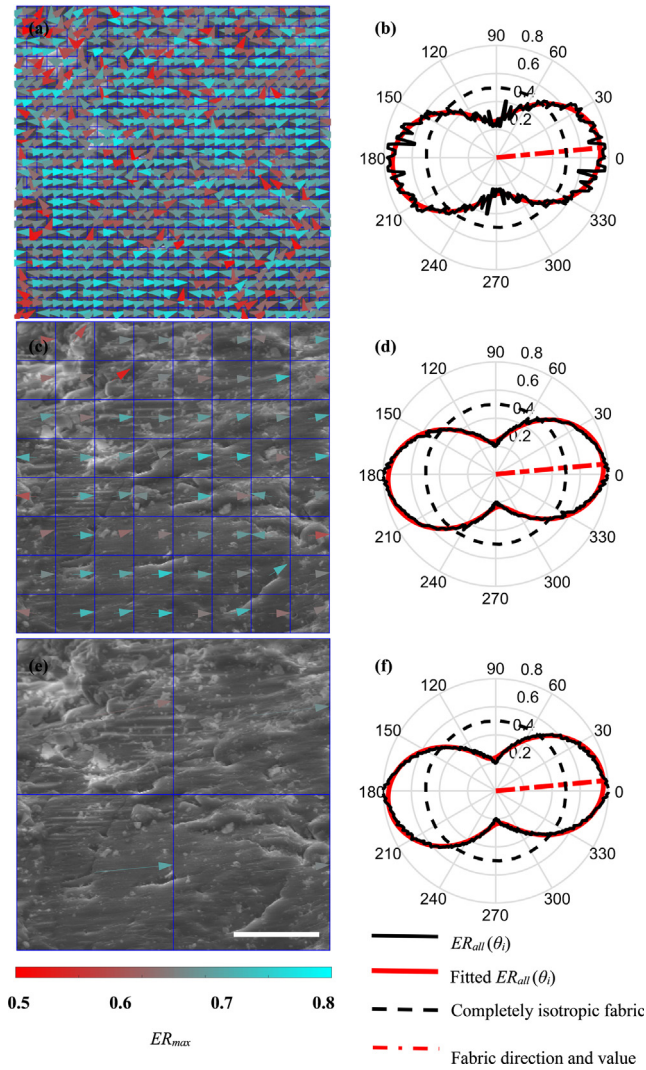
Fig. 6. Multiscale rotational HWT for an intact limestone surface with resolution of about $2^{8.5} \times 2^{8.5}$ pixels: (a), (c) and (e) are with M equal to 3, 5 and 7. The scale bar in it represents 20 μm.

Fig. 7. Multiscale rotational HWT for a fractured limestone surface with resolution of $2^{8.5} \times 2^{8.5}$ pixels: (a), (c) and (e) are with M equal to 4, 6 and 8. The scale bar in it represents 20 μm.

sentative process of multiscale rotational HWT for SEM images of a limestone fracture surface and an intact LBS surface.

4. Results

4.1. Breakage behaviour and mechanical response

4.1.1. Uniaxial compression

Fig. 8 illustrates a representative force–displacement relationship for two LBS particles artificially cemented by gypsum plaster (GPLBS) under uniaxial compression. It could be observed that the curve before the peak is roughly linear in spite of some scatter at beginning. That means vertical force applied on the specimen increases lineally with the increasing of the vertical displacement during tests until a peak value appears, which is about 260 N in this case.

Corresponding to Fig. 8, a series of images illustrating the specimen breakage process under compression is shown in Fig. 9. At point 2, where is prior to the peak force in Fig. 8, a crack occurred along the loading axis inside the upper LBS particle. It is noted that the particle broke with no immediate effects on the force–displacement response. Following the particle failure, a fracture quickly
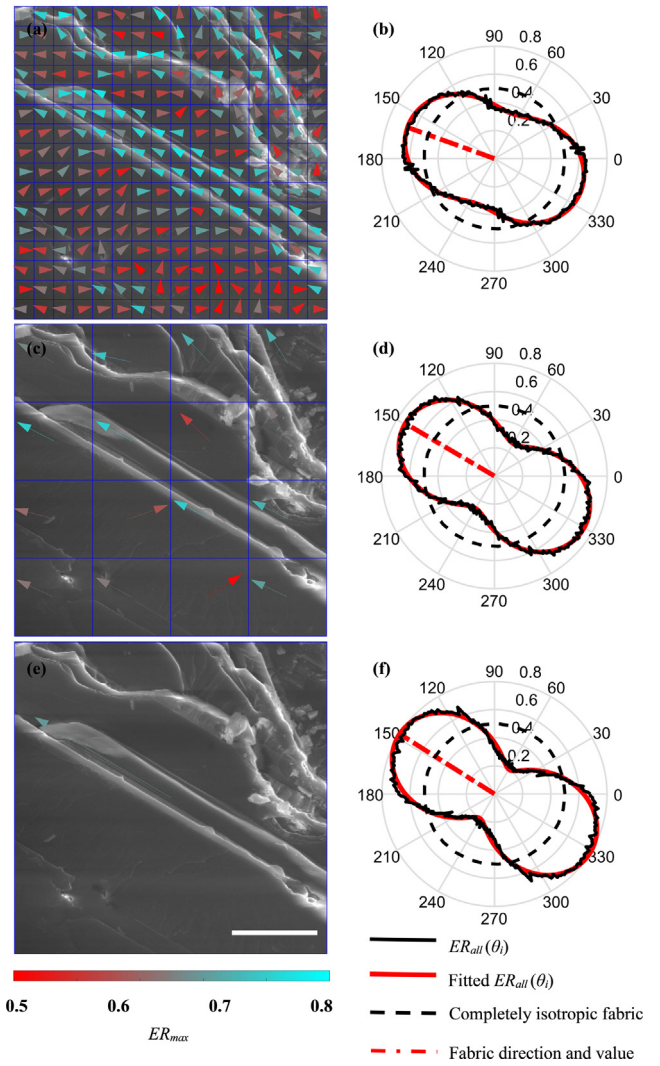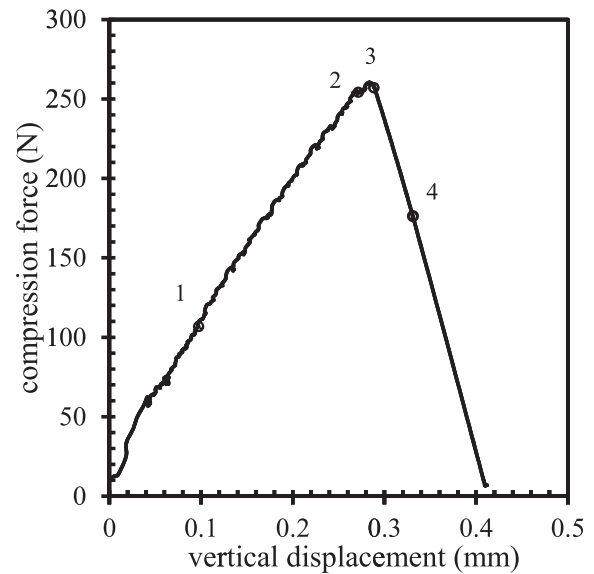

Fig. 8. Relationship between compression force and vertical displacement of a GPLBS during a normal compression test (Data points of 1, 2, 3 and 4 correspond to the images in Fig. 9).
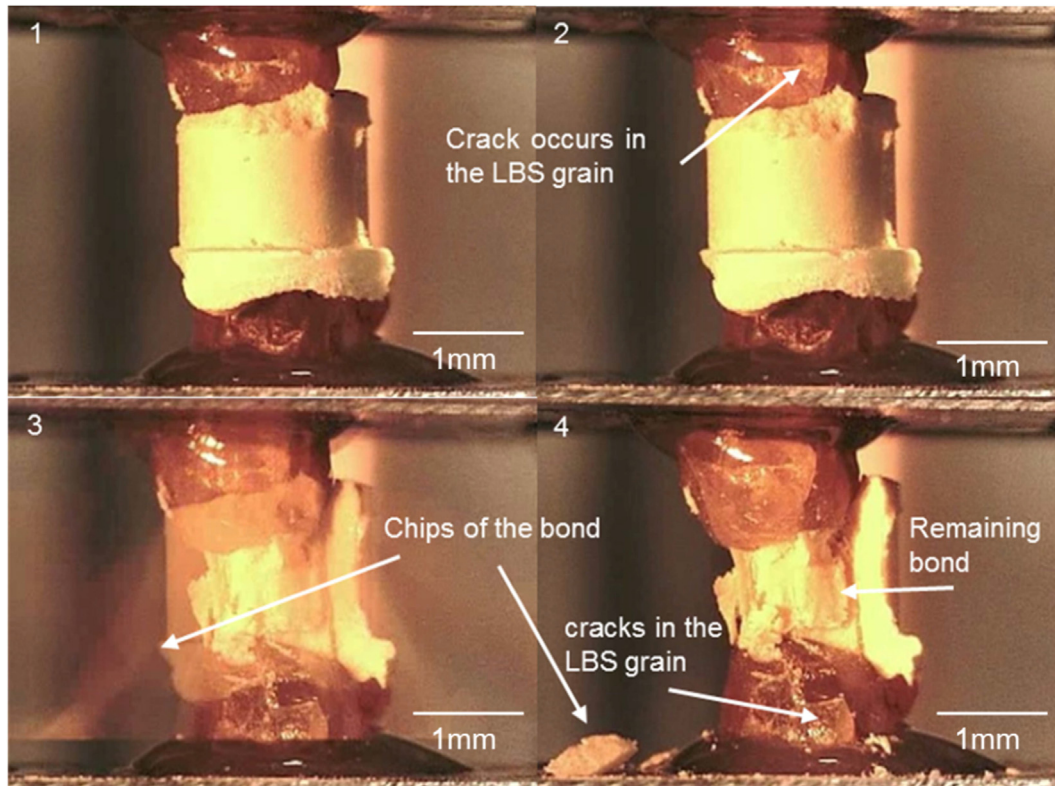
Fig. 9. Breakage behaviour of GPLBS under compression corresponding to Fig. 8.
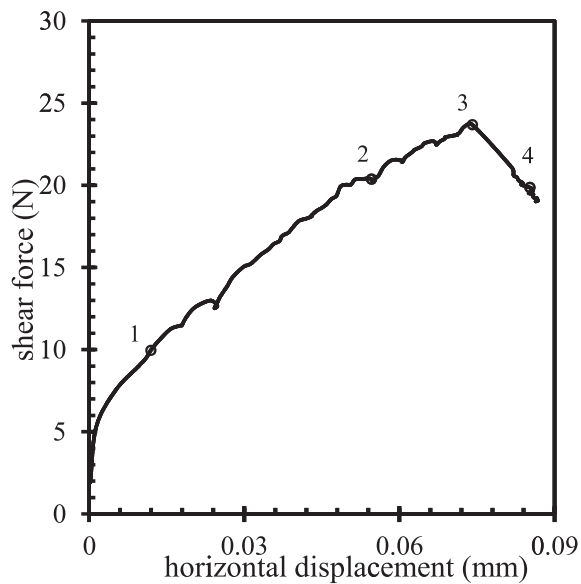

Fig. 10. Relationship between shear force and horizontal displacement of a GPLBS for a pure shear test with no bending and a normal force of 50 N (Data points of 1, 2, 3 and 4 correspond to the images in Fig. 11).

4.1.2. Pure shear

At the beginning of pure shearing test, vertical force with a speed of 2 mm/hour was applied along the vertical axis of GPLBS. Once the force reached 50 N, it turned to be controlled as a constant value using an inhouse control code. The left and right loading ends were adjusted in one horizontal plane, which coincides with the horizontal symmetry plane of the cementation. Then horizontal shear force was gradually applied, in which no bending moment application on the specimen. Fig. 10 presents a represen-
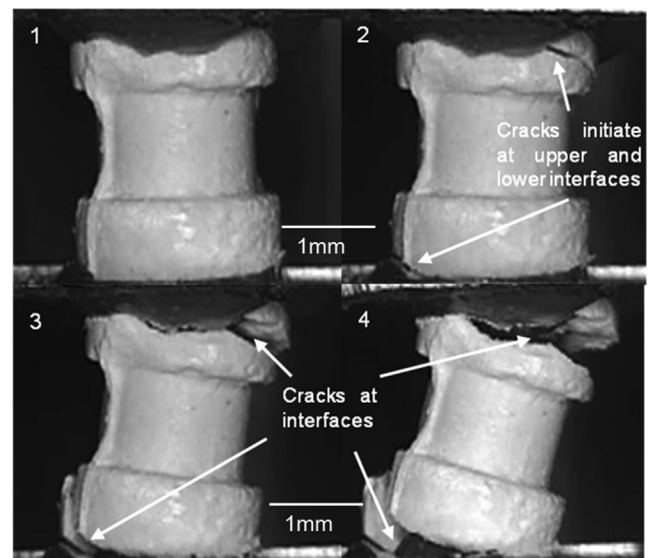

Fig. 11. Breakage behaviour of GPLBS for a pure shear test with no bending corresponding to Fig. 10.

propagated through the bond vertically and a chip split off. This occurred instantaneously, resulting in a sudden drop of the force–displacement curve. After the failure, it could be observed that the lower sand particle also broke in this process, with a part of cementation retaining between two particles and small gypsum plaster chip laying on the lower mount.
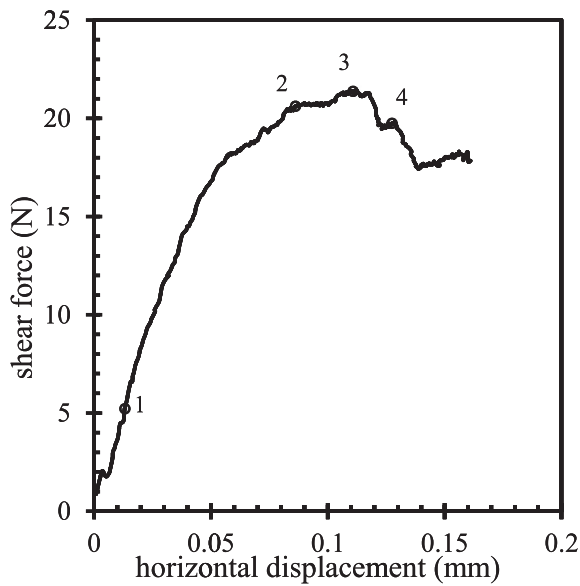
Fig. 12. Relationship between shear force and horizontal displacement of a GPLBS for a bending test with normal force of 50 N (Data points of 1, 2, 3 and 4 correspond to the images in Fig. 13).

tative shear force-horizontal displacement curve for a pure shear test under a constant normal force 50 N without bending moment. At the beginning of the test, the curve shows convex. Then it turns to be linear when the shear force exceeds10N. The curve continues to rise to about 24 N, following with a sudden drop indication the GPLBS fails.

Fig. 11 describes the failure process of GPLBS under pure shearing with a normal force 50 N corresponding to test in Fig. 10. Compared to image at point 1 in initial loading stage, the specimen at point 2 inclines slightly along the horizontal loading direction. Cracks could be observed to initiate at both upper and lower interfaces between cementation and particles. In terms of the mechanical response in Fig. 10, however, the curve seems to be affected

insignificantly by the crack initiation and continues to increase after experiencing a short standstill. At point 3, where the shear force reaches maximum value, cracks at both sides propagate and the cemented grains is more inclined. Thereafter, at point 4, the cracks propagate rapidly. As a result, the particle completely debonds from cementation and no longer carries shear force, corresponding to a sharp decline in the force–displacement curve in Fig. 10.

4.1.3. Bending

Fig. 12 and Fig. 13 illustrate a representative shear force-horizontal displacement curve along with particle images describing breakage process for a compression, shear and bending combined test. In this case, an eccentric distance e_0 1.6 mm for horizontal force was set for application of bending moment. Also, a normal force, e.g. 50 N, was applied first and then set as a constant value to keep the cemented sand vertically stable. The relationship between shear force and horizontal displacement for combined shear and bending tests shows a quite similar trend with that for pure shear tests before failure. However, unlike the sudden drop of shear force after failure in pure shear tests, the curve comes to a softening regime for compression-shear-bending test. That coincides with results from Jiang et al. [23], in which a softening regime was found for the thick bond. It should be noticed that the horizontal displacement in this case consists of two parts: one resulting from rotation of the upper mount, the other resulting from shearing. That's the reason why two LVDTs were assembled symmetrically about load axis in each direction. The displacement caused by shearing is obtained from the average value of the readings from the two LVDTs, which is used in Fig. 12.

From point 1 to point 2, where the shear force gradually increases to about 20 N, the images in Fig. 13 shows no visible crack either in bond or particles. As the shear force reaching to the peak value 21.2 N, one visible inclined crack though the bond has been seen, followed by a slight drop in force. In this case, the cemented grains do not fail completely and continue to carry retaining force. At point 4, which is the second peak value of shear force 19.5 N, two more roughly parallel inclined cracks propagate inside the bond. Among the three cracks, there is longest one
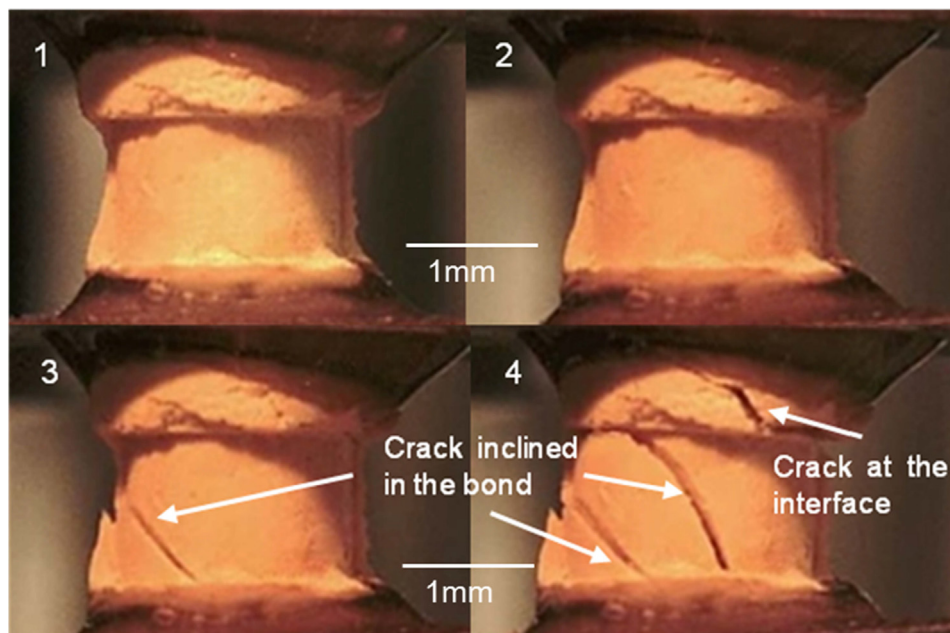

Fig. 13. Breakage behaviour of GPLBS for a bending test corresponding to Fig. 12.
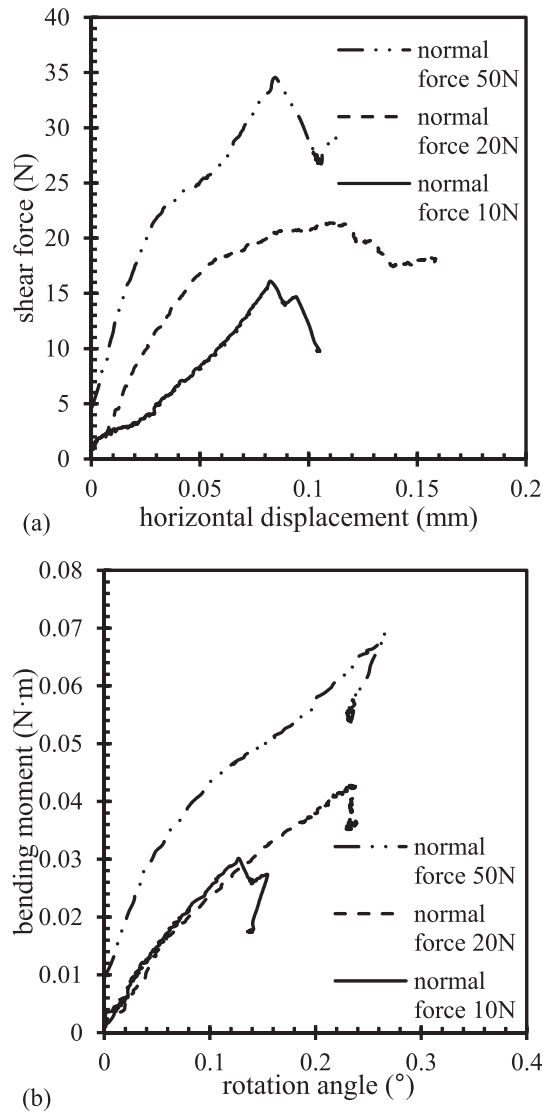
(a)

(b)

Fig. 14. Mechanical response for the bending tests on cemented LBS grains with gypsum plaster under different normal force (a) shear force-horizontal displacement (b) bending moment-rotation angle.

through the whole height of the bond, named major crack. As the major crack occurring and propagating, the shear force decreases remarkably, followed by a softening regime. The retaining of the specimen after failure could continue to carry a certain compressive force. Therefore, the softening regime is actually the compressive softening. The results are consistent with the conclusion of Jiang et al. [23].

Moreover, the influence of constant normal force applied on the cemented grains during normal-shear-bending tests on shearing as well as bending strength was investigated. For the series of tests, the eccentricity of the shear force to the centreline is all equal to 1.6 mm and three different values of constant normal force 10 N, 20 N, and 50 N were applied. Fig. 14(a) illustrates the mechanical response for the combined bending tests under normal force 10 N, 20 N and 50 N in terms of shear force-horizontal displacement curves. When the normal force applied is equal to 10 N, the peak shear force is round 16 N while the displacement at failure is about 0.08 mm. After the first peak, the force decreases slightly to 13.9 N and then continues to rise to the second peak 14.7 N, followed by a remarkable drop. If the normal force increases to 20 N, it is noticed that with the increase of horizontal displacement, the
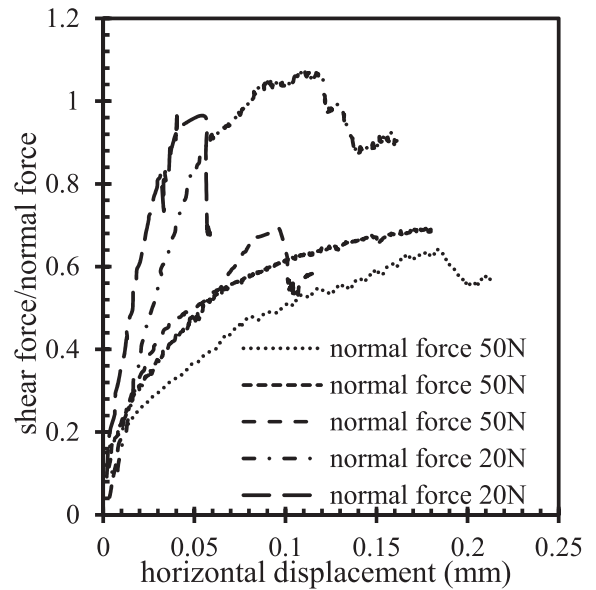

Fig. 15. Ratio of peak shear force over normal force under different normal force for the bending tests on GPLBS.
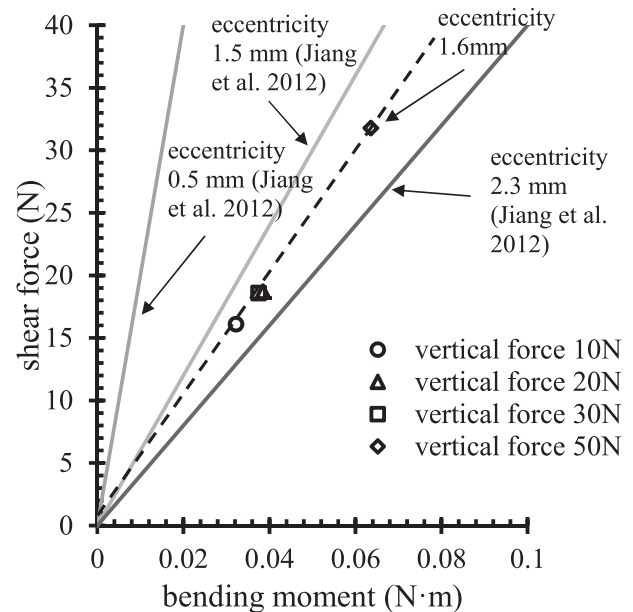

Fig. 16. The relationship between shear force and bending moment for bending tests on LBS cemented particles with gypsum, compared the results from [23].

Table 1
Summarization of SEM properties for Fig. 17.

Number	Type	Pixel size (µm)
(a)	Intact LBS surface	0.870
(b)	Fractured LBS surface	0.870
(c)	Intact limestone surface	0.174
(d)	Fractured limestone surface	0.174
(e)	Horizontal fractured gypsum surface	0.174
(f)	Longitudinal fractured gypsum surface	0.174
(g)	Intact Portland cement surface	0.174
(h)	Longitudinal fractured Portland cement surface	0.174
(i)	Longitudinal fractured Portland cement surface	0.345
(j)	Horizontal fractured Portland cement surface	0.345

increase of shear force becomes obviously slow. After a hardening regime, the shear force reaches to about 21.4 N and then drops to 17 N, turning to a softening regime. When the normal force is equal to 50 N, the trend of the force–displacement relationship is similar to that under normal force of 10 N, and the peak force is 34.4 N with a horizontal displacement of 0.08 mm. Again, after a short decrease to 26.8 N, the shear force continues to go up. In this case, the second peak force was not found, partly because of the short record of the further data. It could be found that with the increase of the normal force, the peak shear force increases for compressive-shear-bending tests. Also, the stiffness of the cemented samples shows an increase tendency with the increase of normal force. However, there is no apparent trend of the horizontal displacement at failure with the variation of the normal force. The relationships of bending moment and rotational angle force the combined bending tests under different normal forces 10, 20 and 50 N are given in Fig. 14(b). It could also be found that the bending moment increases with increase of the normal force, for which the moment values are 0.03, 0.04 and 0.07 N·m corresponding to under normal force 10, 20 and 50 N, respectively. In this case, a roughly positive trend of rotation angle at failure with normal force increasing could be observed.

Fig. 15 illustrates the relationship between the ratio of shear force over normal force and horizontal displacement under different normal force 20 and 50 N for combined bending tests. The curves show that for same normal force, the ratio is quite consistent. If normal force is applied as 20 N, the ratio of shear force over normal force is about 0.75 while that value changes to 1 if the normal force is equal to 50 N. Not only the ratio of shear force over normal force increases with normal force increasing, the slopes of the curve also shows an increasing tendency with normal force increase.

Jiang et al. [23] plotted stress envelops for combined bending tests on cemented aluminium bars in terms of the relationship between shear force and bending moments. Although the figure indicated no clear trend for the effect of the normal force on the shear and moment resistance, the slope of the line for the points connection decreased with the increase of the eccentricity as shown in Fig. 16. In terms of shear force and bending moment, the data points are linear and indicates roughly positive correlations between shear force or bending moment and the normal force. In addition, the connection line of the four data points lying between the two lines for eccentricity of 1.5 and 2.3 mm. In this study, the eccentricity of shear force applied on the cemented particle is about 1.6 mm, which agree well with the conclusion of Jiang et al. It should be pointed that particles in Jiang et al.'s experiments are made of steel, which aims at an ideal case for DEM calibration, thus fractures cannot propagate inside aggregates. Meanwhile, the spherically shaped geometries would not induce high-stress concentration as realistic sand shapes. Refer to our experiments, more advanced combined finite and discrete element method (FDEM, [52]) can be taken into consideration to shed light on micro mechanics phenomenon, to which experiments are not accessible, of cemented sand fracture behaviour.

4.2. Fabric quantification of fracture surfaces

There are 10 SEM images for each intact and fractured LBS, limestone, gypsum and Portland cement surfaces conducting multiscale RHWT. Table 1 summarizes them with SEM properties on the bottom of them in Fig. 17. Notably, for quantitative comparison of fracture-induced surfaces, for one particular material (e.g. LBS, limestone, gypsum and Portland cement) the SEM images are of the same resolution, in terms of pixel size.

Fabric directions are meaningful only when they indicate the directions of the same image with diverse subarea sizes because the SEM images are obtained from a random view rather than in in-situ experiments, where the camera angles were kept the same for all crushing tests of cemented sands. Simultaneously, surface morphology does have multi-scaled features, and thus influence the distribution of ER_{max}, as indicated in Fig. 6(a), (c) and (e), with the increase of subarea sizes tiny features can be smoothed or eliminated. However, tiny morphology characteristics are not considered here, and only rough textures are covered, which means the size of subareas cannot be too small or large because of the fluctuated fabric directions in both ends of black lines in Fig. 18. Hence only fabric of subarea of size 16 pixels is taken into consideration to quantify fabric values.

Specifically, for sand materials, due to crushing LBS surface becomes smoothed as the fabric value decreases from 0.61 to 0.54 for subarea size equal to 16, in Fig. 18(a). As for limestone, striped textures are more distinct than LBS (see Fig. 17). With the increase of subarea size, small-scale morphology features can be filtered, as demonstrated in Fig. 7(a), (c) and (e), which results
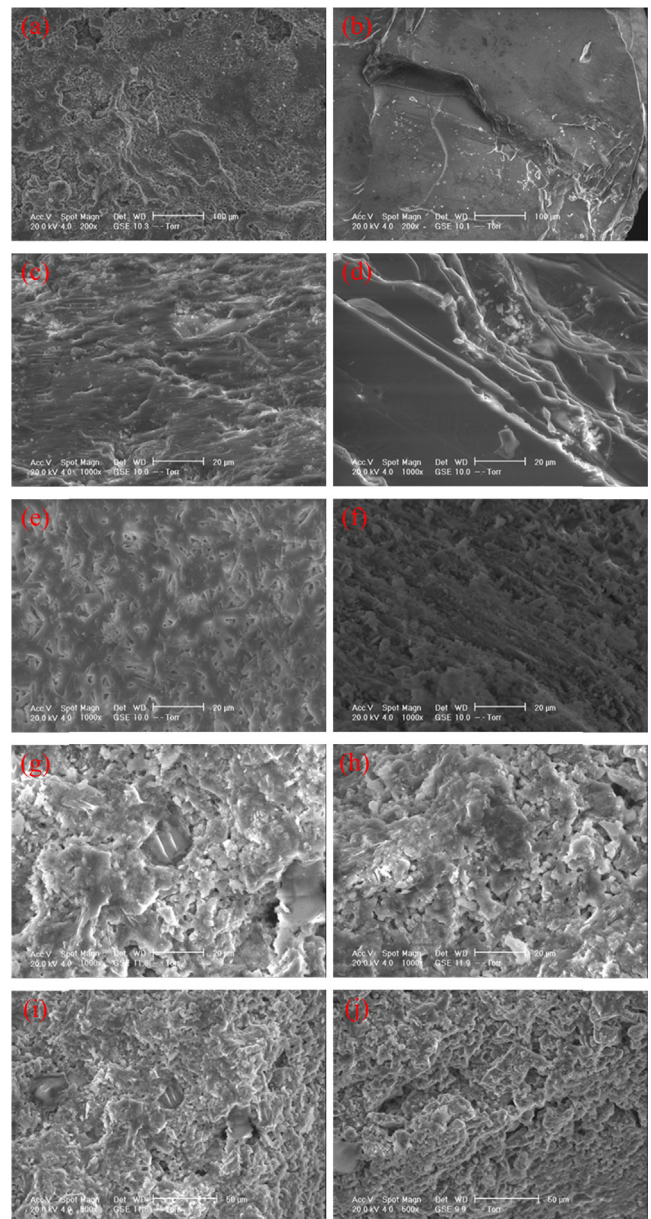

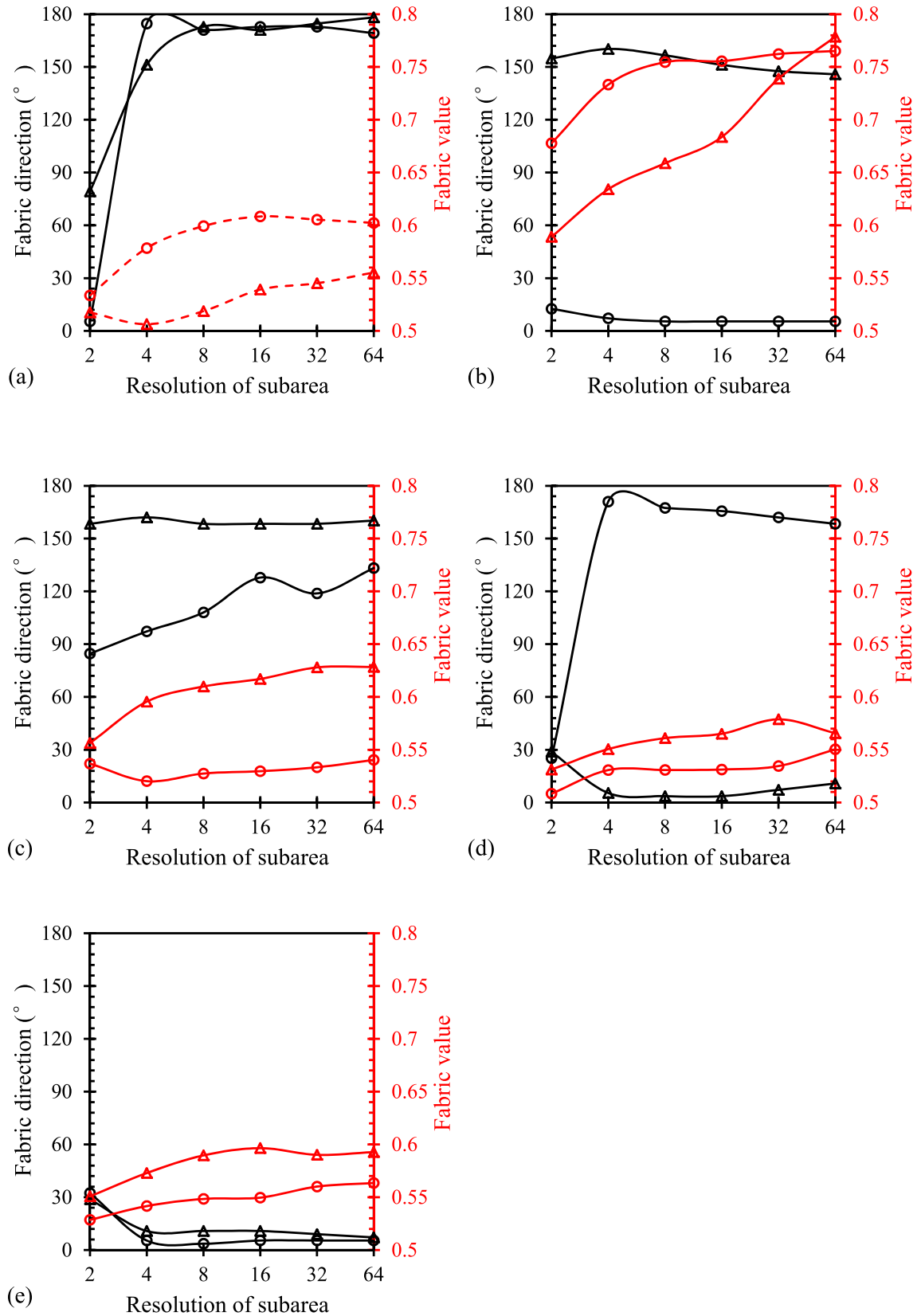**Fig. 17.** SEM images summarized in Table. 1 for multiscale RHWT.

Fig. 18. Fabric directions (black lines) and values (red lines) for intact (lines with circle) and fractured (lines with diamond) LBS surfaces (a), intact (lines with circle) and fractured (lines with diamond) limestone surfaces (b), horizontal (lines with circle) and longitudinal (lines with diamond) fracture surfaces of gypsum (c), intact (lines with circle) and fractured (lines with diamond) surfaces of Portland cement (d), and longitudinal (lines with circle) and horizontal (line with diamond) fractured surfaces of Portland cement (e). (For interpretation of the references to colour in this figure legend, the reader is referred to the web version of this article.)

in higher fabric value (0.78) of its fractured surface than 0.76 of its intact surface, although both introduce more evident fabric than LBS surfaces. Interestingly, the fabric changes of bonded materials, such as Portland cement in Fig. 18(d), are much different from those of sand materials; that is, there is no distinct change occurring due to crushing, as the described in their SEM images in Fig. 17(g) and (h). Meanwhile, the fabric values of horizontal and longitudinal fractured surfaces are contrary for gypsum and Portland cement. The fabric value of longitudinal fractured surface is much larger than that of horizontal fractured surface for gypsum materials, while the fabric of longitudinal fractured surface is, although slightly, smaller than that of horizontal fractured surface.

4.3. Discussion

According to the classical Griffth fracture mechanism, fracture modes can be classified into three modes: tension (mode I), shear (mode II) and slip (mode III). Although in this study three different loading modes are applied, in micromechanics all the fractures are induced by mixed Griffith fracture modes. Meanwhile, seldom are cemented sand in reality fractured from purely single Griffith fracture mechanism. As a result, it is not trivial to merge SEM fabric analysis of fractures from three different loading modes. The focus of this study is on presenting different failure modes induced by various loading conditions and the existence of distinctive fracture surface fabric of composed materials of cemented sands; thus, indicate the insufficiency of current studies in cemented sand breakage for classical geotechnical problems. For example, with the increase of included angles by fabric directions and loading directions of composite material, nominal stresses with the same stretch would evidently decrease [5]. It should also be noted that in this study only SEM images of totally intact or completely fractured surfaces are applied to conduct multiscale rotational HWT. It is reasonable to conduct multi-scale rotational HWT on images mixed with unfractured and fractured surfaces, which can be distinguished by the fabric difference, to extract more fracture features, such as fracture location and fracture width via fabric value, and complex fracture paths via fabric direction.

We also realize the disadvantages of this study; that is, no quantitative relations between fabric tensor and failure mechanism parameters, such as failure stress and elastic modulus. However, our experiments currently do not have enough data for efficiently introducing this, which is ongoing.

5. Conclusion

In this study, real soil grains (e.g. Leighton Buzzard sands, crushed limestone sands) were used to prepare artificially cemented particle samples, which could present slightly cemented or younger clastic rock in nature, according to Jiang et al. [23] as defined as a "thick bond". Gypsum plaster and Portland cement were used as the bond materials. The artificially cemented particles were tested using a novel apparatus under different loading paths, including compression, shear and bending to investigate the mechanical response and the failure behaviour.

The results show that under compression, the compressive force increases roughly linearly with increasing of displacement until a catastrophic failure occur sand cracks along loading axis could be observed in both particles and cementations. For pure shear tests (with a constant compressive load), with increasing of shear force and horizontal displacement, cracks at both interfaces between grains and bond could be found. Detachment of particles from cementation results in the failure in this loading paths. During the combined compressive-shear-bending tests, the mechanical response in terms of shear-displacement curves exhibited a

hardening regime before the peak force and then turned into a softening regime with a residual stress. Inclined cracks initiated and propagated in the cementation in this case. Also for combined bending tests, with the increasing of normal force, peak shear force, bending moment at failure as well as the ratio of shear force over normal force could increase, respectively.

For compressive tests, the samples before and after tests were scanned using scanning electron microscope (SEM) and a fabric quantification method for cemented sand fracture surface was proposed. Since cracks could initiate in both sand particles and cementation in this loading path, generated fracture surface tomography features are rather different, especially for different materials. Using a newly defined fabric tensor based on rotational Haar Wavelet transformation (HWT) performed on subareas of SEM images, the change of fabric could be described quantitatively, and the compressing-induced fracture surfaces could be automatically characterized rather than by vague human cognition. More interesting results sufficiently indicating the dependence of failure modes on fracture surface fabric, as well as influences of fracture surface fabric tensor on fracture stress and elastic modulus can be obtained by large number of experimental.

CRediT authorship contribution statement

Wanying Wang: Methodology, Validation, Formal analysis, Investigation, Resources, Data curation, Writing - original draft, Visualization, Project administration, Funding acquisition. **Deheng Wei:** Conceptualization, Software, Methodology, Validation, Formal analysis, Investigation, Data curation, Writing - original draft, Visualization. **Yixiang Gan:** Validation, Writing - review & editing, Visualization, Supervision.

Declaration of Competing Interest

The authors declare that they have no known competing financial interests or personal relationships that could have appeared to influence the work reported in this paper.

Acknowledgement

References

[1] D.W. Airey, Triaxial testing of naturally cemented carbonate soil, J. Geotech. Eng. 119 (9) (1993) 1379–1398.
[2] S.M. Al-Thawadi, Ureolytic bacteria and calcium carbonate formation as a mechanism of strength enhancement of sand, J. Adv. Sci. Eng. Res 1 (1) (2011) 98–114.
[3] C.A. Anagnostopoulos, Laboratory study of an injected granular soil with polymer grouts, Tunn. Undergr. Space Technol. 20 (6) (2005) 525–533.
[4] D. André, J. Girardot, C. Hubert, A novel DEM approach for modeling brittle elastic media based on distinct lattice spring model, Comput. Methods Appl. Mech. Eng. 350 (2019) 100–122.
[5] L. Astruc, A. Morch, J.F. Witz, V. Nováček, F. Turquier, T. Hoc, M. Brieu, An anisotropic micro-ellipsoid constitutive model based on a microstructural description of fibrous soft tissues, J. Mech. Phys. Solids 131 (2019) 56–73.
[6] M.A. Celigueta, S. Latorre, F. Arrufat, E. Oñate, Accurate modelling of the elastic behavior of a continuum with the Discrete Element Method, Comput. Mech. 60 (6) (2017) 997–1010.
[7] M.R. Coop, J.H. Atkinson, The mechanics of cemented carbonate sands, Geotechnique 43 (1) (1993) 53–67.
[8] M.R. Coop, S.M. Willson, Behavior of hydrocarbon reservoir sands and sandstones, J. Geotech. Geoenviron. Eng. 129 (11) (2003) 1010–1019.
[9] C. Chandan, K. Sivakumar, E. Masad, T. Fletcher, Application of imaging techniques to geometry analysis of aggregate particles, J. Comput. Civil Eng. 18 (1) (2004) 75–82.
[10] L.Y.G. Cheung, C. Osullivan, M.R. Coop, Discrete element method simulations of analogue reservoir sandstones, Int. J. Rock Mech. Min. Sci. 63 (2013) 93–103.
[11] T. Cuccovillo, M.R. Coop, On the mechanics of structured sands, Géotechnique 49 (6) (1999) 741–760.

[12] C. Dano, P.Y. Hicher, Behavior of uncemented sands and grouted sands before peak strength, Soils Found. 43 (4) (2003) 13–19.

[13] J.P. de Bono, G.R. McDowell, Discrete element modelling of one-dimensional compression of cemented sand, Granular Matter 16 (1) (2014) 79–90.

[14] N. Estrada, A. Lizcano, A. Taboada, Simulation of cemented granular materials. I. Macroscopic stress-strain response and strain localization, Phys. Rev. E 82 (1) (2010) 011303.

[15] N. Estrada, A. Lizcano, A. Taboada, Simulation of cemented granular materials. II. Micromechanical description and strength mobilization at the onset of macroscopic yielding, Phys. Rev. E 82 (1) (2010) 011304.

[16] I. Einav, Breakage mechanics—part I: theory, J. Mech. Phys. Solids 55 (6) (2007) 1274–1297.

[17] Z. Gao, J. Zhao, Constitutive modeling of artificially cemented sand by considering fabric anisotropy, Comput. Geotech. 41 (2012) 57–69.

[18] A. Haar, Zur theorie der orthogonalen funktionensysteme, Math. Ann. 69 (3) (1910) 331–371.

[19] P.Y. Hicher, C.S. Chang, C. Dano, Multi-scale modeling of grouted sand behavior, Int. J. Solids Struct. 45 (16) (2008) 4362–4374.

[20] J.T. Huang, D.W. Airey, Properties of artificially cemented carbonate sand, J. Geotech. Geoenviron. Eng. 124 (6) (1998) 492–499.

[21] R.C. Hurley, D.C. Pagan, An in-situ study of stress evolution and fracture growth during compression of concrete, Int. J. Solids Struct. 168 (2019) 26–40.

[22] M.J. Jiang, H.B. Yan, H.H. Zhu, S. Utili, Modeling shear behavior and strain localization in cemented sands by two-dimensional distinct element method analyses, Comput. Geotech. 38 (1) (2011) 14–29.

[23] M.J. Jiang, Y.G. Sun, L.Q. Li, H.H. Zhu, Contact behavior of idealized granules bonded in two different interparticle distances: An experimental investigation, Mech. Mater. 55 (2012) 1–15.

[24] K. Kasama, K. Zen, K. Iwataki, Undrained shear strength of cement-treated soils, Soils Found. 46 (2) (2006) 221–232.

[25] R. Lagioia, R. Nova, An experimental and theoretical study of the behaviour of a calcarenite in triaxial compression, Géotechnique 45 (4) (1995) 633–648.

[26] E.N. Landis, E.N. Nagy, D.T. Keane, Microstructure and fracture in three dimensions, Eng. Fract. Mech. 70 (7–8) (2003) 911–925.

[27] S. Leroueil, P.R. Vaughan, The general and congruent effects of structure in natural soils and weak rocks, Géotechnique 40 (3) (1990) 467–488.

[28] S.C. Lo, P.V. Lade, S.P.R. Wardani, An experimental study of the mechanics of two weakly cemented soils, Geotech. Test. J. 26 (3) (2003) 328–341.

[29] E. Masad, B. Muhunthan, N. Shashidhar, T. Harman, Internal structure characterization of asphalt concrete using image analysis, J. Comput. Civil Eng. 13 (2) (1999) 88–95.

[30] J.K. Mitchell, K. Soga, Fundamentals of Soil Behavior, John Wiley & Sons, Hoboken, NJ, 2005.

[31] R. Nova, R. Castellanza, C. Tamagnini, A constitutive model for bonded geomaterials subject to mechanical and/or chemical degradation, Int. J. Numer. Anal. Meth. Geomech. 27 (9) (2003) 705–732.

[32] H.S. Ohm, R.D. Hryciw, Size distribution of coarse-grained soil by sedimaging, J. Geotech. Geoenviron. Eng. 140 (4) (2013) 04013053.

[33] F.J. Pettijohn, P.E. Potter, R. Siever, Sand and Sandstone, Springer Science & Business Media, 2012.

[34] D.O. Potyondy, P.A. Cundall, A bonded-particle model for rock, Int. J. Rock Mech. Min. Sci. 41 (8) (2004) 1329–1364.

[35] K.R. Reddy, S.K. Saxena, Constitutive modeling of cemented sand, Mech. Mater. 14 (2) (1992) 155–178.

[36] S.K. Saxena, K.R. Reddy, A.S. Avramidis, Liquefaction resistance of artificially cemented sand, J. Geotech. Eng. 114 (12) (1988) 1395–1413.

[37] Z. Shen, M. Jiang, C. Thornton, DEM simulation of bonded granular material. Part I: contact model and application to cemented sand, Comput. Geotech. 75 (2016) 192–209.

[38] S. Shin, R.D. Hryciw, Wavelet analysis of soil mass images for particle size determination, J. Comput. Civ. Eng. 18 (1) (2004) 19–27.

[39] A. Tengattini, A. Das, G.D. Nguyen, G. Viggiani, S.A. Hall, I. Einav, A thermomechanical constitutive model for cemented granular materials with quantifiable internal variables. Part I—Theory, J. Mech. Phys. Solids 70 (2014) 281–296.

[40] V. Topin, J.Y. Delenne, F. Radjaı, L. Brendel, F. Mabille, Strength and failure of cemented granular matter, Eur. Phys. J. E 23 (4) (2007) 413–429.

[41] W. Wang, V. Nardelli, M.R. Coop, The micro-mechanical behaviour of artificially cemented sand particles under compression and shear, Géotechnique Lett. 7 (3) (2017) 1–7.

[42] W. Wang, M.R. Coop, K. Senetakis, The Development of a micromechanical apparatus applying combined normal–shear–bending forces to natural sand grains with artificial bonds, Geotech. Test. J. 42 (4) (2018) 1090–1099.

[43] Y.H. Wang, S.C. Leung, A particulate-scale investigation of cemented sand behavior, Can. Geotech. J. 45 (1) (2008) 29–44.

[44] Y.H. Wang, S.C. Leung, Characterization of cemented sand by experimental and numerical investigations, J. Geotech. Geoenviron. Eng. 134 (7) (2008) 992–1004.

[45] T.F. Wong, L.C. Wu, Tensile stress concentration and compressive failure in cemented granular material, Geophys. Res. Lett. 22 (13) (1995) 1649–1652.

[46] J. Xiao, J. Li, C. Zhang, Mechanical properties of recycled aggregate concrete under uniaxial loading, Cem. Concr. Res. 35 (6) (2005) 1187–1194.

[47] L. Yang, E. Yilmaz, J. Li, H. Liu, H. Jiang, Effect of superplasticizer type and dosage on fluidity and strength behavior of cemented tailings backfill with different solid contents, Constr. Build. Mater. 187 (2018) 290–298.

[48] Y. Yu, J. Pu, K. Ugai, A damage model for soil-cement mixture, Soils Found. 38 (3) (1998) 1–12.

[49] C. Zhai, D.C. Pagan, R.C. Hurley, In situ X-ray tomography and 3D X-ray diffraction measurements of cemented granular materials, JOM (2019) 1–10.

[50] J. Zheng, R.D. Hryciw, Particulate material fabric characterization by rotational haar wavelet transform, Comput. Geotech. 88 (2017) 46–60.

[51] J. Zheng, R.D. Hryciw, Cross-anisotropic fabric of sands by wavelet-based simulation of human cognition, Soils Found. 58 (4) (2018) 1028–1041.

[52] D. Wei, B. Zhao, D. Dias-da-Costa, Y. Gan, An FDEM study of particle breakage under rotational point loading, Engineering Fracture Mechanics 212 (2019) 221–237.